The Astrophysical Journal, 995:95 (14pp), 2025 December 10 https://doi.org/10.3847/1538-4357/ae17c8

Magma Ocean Interactions Can Explain JWST Observations of the Sub-Neptune TOI-270 d

Matthew C. Nixon[1,2,10], R. Sander Somers[2], Arjun B. Savel[2], Jegug Ih[3], Eliza M.-R. Kempton[2,4], Edward D. Young[5], Hilke E. Schlichting[5], Tim Lichtenberg[6], Luis Welbanks[1], William Misener[7], Anjali A. A. Piette[8], and Nicholas F. Wogan[9]
[1] School of Earth and Space Exploration, Arizona State University, Tempe, AZ, USA; matthewnixon@asu.edu
[2] Department of Astronomy, University of Maryland, College Park, MD, USA
[3] Space Telescope Science Institute, 3700 San Martin Drive, Baltimore, MD, USA
[4] Department of Astronomy & Astrophysics, University of Chicago, Chicago, IL, USA
[5] Department of Earth, Planetary, and Space Sciences University of California, Los Angeles, CA, USA
[6] Kapteyn Astronomical Institute, University of Groningen, Groningen, The Netherlands
[7] Earth and Planets Laboratory, Carnegie Institution for Science, Washington, DC, USA
[8] School of Physics and Astronomy, University of Birmingham, Edgbaston, Birmingham, UK
[9] Space Science Division, NASA Ames Research Center, Moffett Field, CA, USA
Received 2025 June 30; revised 2025 October 21; accepted 2025 October 24; published 2025 December 9

Abstract

Sub-Neptunes with substantial atmospheres may possess magma oceans in contact with the overlying gas, with chemical interactions between the atmosphere and magma playing an important role in shaping atmospheric composition. Early JWST observations have found high abundances of carbon- and oxygen-bearing molecules in a number of sub-Neptune atmospheres, which may result from processes including accretion of icy material at formation or magma–atmosphere interactions. Previous work examining the effects of magma–atmosphere interactions on sub-Neptunes has mostly been limited to studying conditions at the atmosphere–mantle boundary, without considering implications for the upper atmosphere, which is probed by spectroscopic observations. In this work, we present a modeling architecture to determine observable signatures of magma–atmosphere interactions. We combine an equilibrium chemistry code which models reactions between the core, mantle, and atmosphere with a radiative–convective model that determines the composition and structure of the observable upper atmosphere. We examine how different conditions at the atmosphere–mantle boundary and different core and mantle compositions impact the upper atmospheric composition. We compare our models to JWST NIRISS + NIRSpec observations of the sub-Neptune TOI-270 d, finding that our models can provide a good fit to the observed transmission spectrum with little fine-tuning. This suggests that magma–atmosphere interactions may be sufficient to explain the high abundances of molecules such as H_2O, CH_4, and CO_2 in sub-Neptune atmospheres, without additional accretion of icy material from the protoplanetary disk. Although other processes could lead to similar compositions, our work highlights the need to consider magma–atmosphere interactions when interpreting the observed atmospheric composition of a sub-Neptune.

Unified Astronomy Thesaurus concepts: Exoplanet structure (495); Exoplanet evolution (491); Exoplanet atmospheric composition (2021); Exoplanet formation (492); Exoplanet atmospheres (487); Exoplanets (498)

1. Introduction

Determining the characteristics of exoplanets whose radii lie between those of the Earth and Neptune (1–4 $R_\oplus$) is one of the major outstanding challenges in the study of exoplanets today. The very existence of these planets is intriguing, since no analogs for such objects exist in our solar system. Statistical trends determined from demographic studies of this population have provided some initial insight into their possible compositions. Planets with radii less than 4 $R_\oplus$ orbiting FGK stars have a bimodal radius distribution (B. J. Fulton et al. 2017), suggestive of two subpopulations, often labeled "super-Earths" ($R_p \lesssim 1.8\ R_\oplus$) and "sub-Neptunes" ($R_p \gtrsim 1.8\ R_\oplus$). It has been suggested that super-Earths are typically rocky bodies with little to no atmosphere, while sub-Neptunes are planets with large H and He atmospheres comprising up to a few percent of their total mass (e.g., H. Chen & L. A. Rogers 2016). However, the range of bulk compositions that can explain the masses and radii of sub-Neptunes is far from unique; for example, a significant number of sub-Neptunes orbiting M dwarf stars appear to be consistent with a water-rich, as well as a hydrogen-rich, atmosphere (R. Luque & E. Pallé 2022; J. G. Rogers et al. 2023).

JWST is transforming our ability to understand the composition of sub-Neptunes by directly probing their atmospheres. Although only a small number of such planets have been observed to date, a wide compositional diversity has been revealed. A number of sub-Neptune observations have revealed high-metallicity (>100 × solar) or water-dominated atmospheres, such as GJ 1214 b (P. Gao et al. 2023; E. M. R. Kempton et al. 2023b; M. C. Nixon et al. 2024b; E. Schlawin et al. 2024), GJ 3470 b (T. G. Beatty et al. 2024), and GJ 9827 d (C. Piaulet-Ghorayeb et al. 2024). However, other sub-Neptune atmospheres appear to be H- and He-dominated, and consistent with solar metallicity (e.g., TOI-421 b; B. Davenport et al. 2025).

[10] 51 Pegasi b Fellow.

This diversity prompts further investigation into the physical and chemical processes that shape the atmospheres of these objects. Note that, in this work, we use the term "metallicity" to refer to the abundance of elements heavier than H and He in the (observable) upper atmosphere.

The sub-Neptune TOI-270 d (M. N. Günther et al. 2019) provides a particularly informative case study thanks to its early observational campaigns with JWST (GO #3557, PI: Madhusudhan; GO #3818, PI: Gapp; and GO #4098, PI: Benneke). The NIRISS/SOSS and NIRSpec G395H transmission spectra of the planet (B. Benneke et al. 2024; M. Holmberg & N. Madhusudhan 2024) enabled detections of CH_4, CO_2, and H_2O in its atmosphere, with a metallicity of $225^{+98}_{-86}\times$ solar derived by B. Benneke et al. (2024) from an analysis of the entire spectrum. This metal-rich composition could be a result of the planet forming further out in the disk, beyond the ice line, and thus accreting more icy material before moving inwards to its present orbital location (C. Mordasini et al. 2009), or of late-stage pollution by icy planetesimals (T. Lichtenberg & M. S. Clement 2022). However, it is also possible that evolutionary processes could enrich the metallicity of an initially H- and He-dominated atmosphere, without invoking an ice-rich interior. Such processes include photoevaporation (J. E. Owen & Y. Wu 2017; K. Heng et al. 2025), core-powered mass loss (A. Gupta & H. E. Schlichting 2019; C. Cherubim et al. 2025), and interaction between the atmosphere and a magma ocean (E. S. Kite et al. 2020; T. Lichtenberg 2021; H. E. Schlichting & E. D. Young 2022), the latter being the focus of this work.

Sub-Neptunes with rocky interiors and terrestrial planets are expected to possess magma oceans (molten silicate layers) in contact with their atmosphere for a substantial portion of their lifetime (L. Schaefer et al. 2016; E. S. Kite et al. 2019; H. Nicholls et al. 2024; Y. Tang et al. 2025). Chemical interactions between the molten core and mantle and the gaseous atmosphere can significantly alter the composition of all components (T. Lichtenberg & Y. Miguel 2025). For sub-Neptunes, this process is expected to lead to oxidation of the atmosphere and reduction of the core and mantle (H. E. Schlichting & E. D. Young 2022), as well as a decrease in the atmospheric carbon-to-oxygen ratio (C/O; C. Seo et al. 2024). The studies mentioned here focused on determining the composition at the base of the atmosphere, rather than the upper atmosphere that may be probed by spectroscopic observations. Additional processes, such as thermochemical equilibrium at pressures lower than that of the atmosphere–mantle boundary, as well as condensation, vertical mixing, and photochemistry, must be considered if we are to test the observable consequences of interactions taking place in planetary interiors.

Motivated by the arrival of JWST observations of sub-Neptunes, efforts are now underway to connect the composition at the base of the atmosphere derived from magma ocean models to the observable upper atmosphere. To date, this work has primarily focused on explaining observations of the sub-Neptune K2-18 b, which has been hypothesized to host a liquid water ocean beneath its atmosphere (e.g., N. Madhusudhan et al. 2020, 2023; M. C. Nixon & N. Madhusudhan 2021). O. Shorttle et al. (2024) found that invoking a magma ocean could explain the apparent depletion of nitrogen in the planet's atmosphere, which had previously been used as a line of evidence for a liquid water ocean (R. Hu et al. 2021; S.-M. Tsai et al. 2021; X. Yu et al. 2021). However, F. E. Rigby et al. (2024) found that a magma ocean was not consistent with observations of K2-18 b, arguing that the magma ocean models are in tension with the bulk parameters of the planet. Regardless of the final interpretation, these works demonstrate the possibility of connecting equilibrium chemistry models of the core, mantle, and base of the atmosphere to the upper atmospheric composition, thus enabling the use of atmospheric compositional constraints from spectroscopy to better understand interior processes in sub-Neptunes. For TOI-270 d, although the possibility of a magma ocean has been suggested (e.g., B. Benneke et al. 2024; C. R. Glein et al. 2025), models predicting the atmospheric composition resulting from magma ocean interactions are yet to be constructed.

In this paper, we develop a new framework for connecting predictions of the composition at the base of the atmosphere from the model presented in H. E. Schlichting & E. D. Young (2022) to the expected upper atmospheric composition. In particular, we are interested in determining whether magma ocean interactions are sufficient to explain the observed upper atmospheric properties of TOI-270 d. In Section 2, we describe our methodology in detail, including our choice of modeling approaches for upper atmospheric processes. We present resulting temperature and volume mixing ratio profiles, as well as a direct comparison to observations of TOI-270 d, in Section 3. Finally, we discuss caveats and possible future developments in Section 4.

2. Methods

Our modeling framework is shown in Figure 1. We use the model described in H. E. Schlichting & E. D. Young (2022) to calculate chemical equilibrium between the core, mantle, and atmosphere. This informs our inputs to `HELIOS` (M. Malik et al. 2017), which we use to simulate atmospheric temperature profiles. We iterate between `HELIOS` and FASTCHEM COND (J. W. Stock et al. 2022), which solves for equilibrium chemistry including rainout condensation, until converged temperature and chemical abundance profiles are obtained. We subsequently model photochemistry and vertical mixing using `Photochem` (N. F. Wogan et al. 2023) before generating transmission spectra with AURA-3D (M. C. Nixon & N. Madhusudhan 2022). We describe each step in more detail below.

2.1. Magma Ocean–Atmosphere Chemical Interactions

H. E. Schlichting & E. D. Young (2022) presented an equilibrium thermodynamic model for sub-Neptunes that accounts for chemical interactions between an iron-rich core, silicate mantle, and hydrogen-rich atmosphere. We use this model to determine the composition at the atmosphere–mantle boundary, which informs our upper atmospheric model. This model uses a variety of sources of thermodynamic data in order to calculate standard-state molar Gibbs free energies of reaction, including B. Fegley & A. G. W. Cameron (1987), V. Pan et al. (1991), T. Okuchi (1997), G. Moore et al. (1998), M. M. Hirschmann et al. (2012), J. Badro et al. (2015), and M. M. Hirschmann (2016). Details on which sources were used for each chemical reaction in the model may be found in the appendix of H. E. Schlichting & E. D. Young (2022).

We adopt planetary parameters similar to those of TOI-270 d, whose total iron and silicate mass fraction was

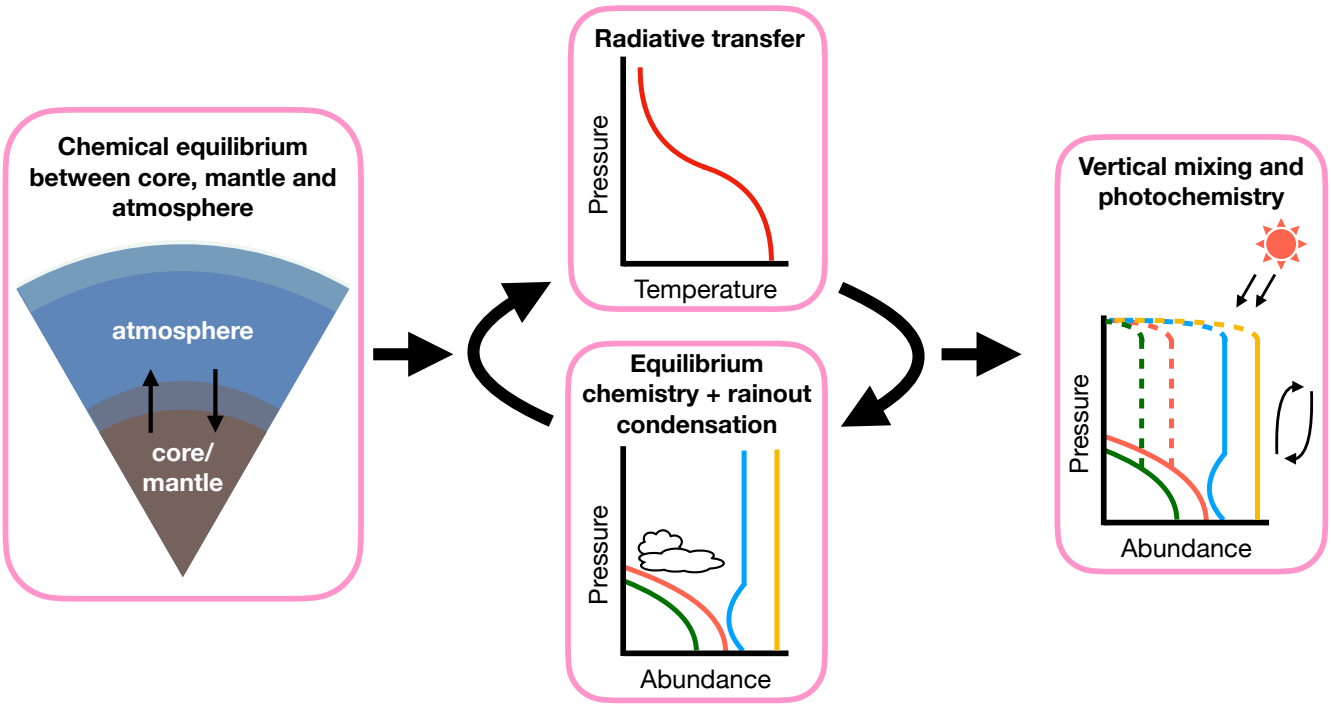

Figure 1. Schematic of the modeling framework used in this study. Chemical equilibrium between the core, mantle, and atmosphere is calculated using the model from H. E. Schlichting & E. D. Young (2022). Upper atmospheric temperature profiles are calculated using HELIOS (M. Malik et al. 2017). FASTCHEM COND (J. W. Stock et al. 2022) is used to find equilibrium chemical abundances throughout the upper atmosphere, accounting for rainout condensation. After iterating between HELIOS and FASTCHEM COND until convergence is reached, we account for photochemical processes and vertical mixing using Photochem (N. F. Wogan et al. 2023, 2025).

determined to be about 90% ($4.3 \pm 0.5\ M_\oplus$) of its total mass, $4.78 \pm 0.43\ M_\oplus$ (V. Van Eylen et al. 2021; B. Benneke et al. 2024). We therefore adopt a total iron and silicate mass of 4.3 $M_\oplus$. We also test the sensitivity of our results to the exact iron plus silicate mass (see Section 3.3). Following H. E. Schlichting & E. D. Young (2022), we consider a reactive core consisting of pure Fe beneath a silicate mantle consisting of 92.1% $MgSiO_3$, 3.5% $FeSiO_3$, and 3.2% MgO by mole fraction, with trace amounts of Na_2O, SiO_2, Na_2SiO_3, and FeO. These components react with an atmosphere consisting of approximately solar composition (M. Asplund et al. 2009) with the following volume mixing ratios: ~99.9% H_2; 0.05% CO and H_2O; 10^{-7} CO_2 and CH_4; and 10^{-9} O_2, Fe, Mg, Na, SiO, and SiH_4. Since He is not included in the model from H. E. Schlichting & E. D. Young (2022), and is generally unreactive, we do not include it at this stage of the modeling, but introduce He at solar abundance in our radiative–convective models of the upper atmosphere.

We construct a grid of models by varying three different input parameters: $T_{\rm m-a}$, the equilibration temperature at the mantle–atmosphere boundary; $T_{\rm c-m}$, the equilibration temperature at the core–mantle boundary; and $x_{\rm Fe}$, the iron mass fraction of the (molten) iron + silicate nucleus of the planet ($x_{\rm Fe} = m_{\rm Fe}/(m_{\rm Fe} + m_{\rm silicates})$). We consider three combinations of temperatures at the mantle–atmosphere and core–mantle boundaries: (1) $T_{\rm m-a} = 2000$ K and $T_{\rm c-m} = 3000$ K; (2) $T_{\rm m-a} = 2000$ K and $T_{\rm c-m} = 4000$ K; and (3) $T_{\rm m-a} = 3000$ K and $T_{\rm c-m} = 4000$ K (see Table 1). The choice of temperatures was motivated by extending an adiabatic temperature profile from the base (1000 bar) of a HELIOS model with parameters consistent with observations of TOI-270 d (B. Benneke et al. 2024) to likely pressures at the base of the atmosphere

Table 1
Ranges of Values Considered for the Parameters Which Are Varied in This Study

Parameter (Unit)	Range
$T_{\rm m-a}$ (K)	2000–3000
$T_{\rm c-m}$ (K)	3000–4000
$x_{\rm Fe}$ (%)	1–50
K_{zz} ($\rm cm^2\ s^{-1}$)	10^3–10^9

Note. $T_{\rm m-a}$, $T_{\rm c-m}$, and $x_{\rm Fe}$ are inputs to the core–mantle–atmosphere equilibrium chemistry model (H. E. Schlichting & E. D. Young 2022), and K_{zz} is an input to the photochemical model (N. Wogan 2024).

(~6×10^4 bar; H. E. Schlichting & E. D. Young 2022), accounting for the wide uncertainty in the temperature gradient and location of the mantle–atmosphere and core–mantle boundaries. For this initial model, we assumed an atmospheric metallicity of 200 × solar, with solar C/O, and all other parameters equal to those described in Section 2.3. We note that temperatures much higher than 5000 K are possible at the core–mantle boundary (S. Ginzburg et al. 2016); however, calculations at such high temperatures would require unreasonable extrapolation of experimental data (H. E. Schlichting & E. D. Young 2022). We also consider several values of $x_{\rm Fe}$: 50%, 33%, 20%, and 1%.

2.2. Upper Atmospheric Chemistry

The output of the global chemical equilibrium code described above includes the volume mixing ratios for a range of chemical species in the atmosphere after interactions with the core and mantle. This represents the composition at the

base of the atmosphere, which for sub-Neptunes is likely to be located at pressures $\gtrsim 1000$ bar, and possibly as high as $\gtrsim 10^6$ bar (B. Breza et al. 2025). However, it is unlikely that this is the same as the composition throughout the upper, observable region of the atmosphere ($P \lesssim 1$ bar) for several reasons described below. The lower pressures and temperatures of the atmosphere will lead to different chemical species being favored in thermochemical equilibrium for a given set of elemental abundances. Furthermore, several of the gas-phase species present in the hot, high-pressure region of the atmosphere (e.g., SiH_4; W. Misener et al. 2023) may condense into solid or liquid phases before reaching the observable atmosphere. Finally, photochemistry and vertical mixing will alter the atmospheric composition near the top of the atmosphere away from thermochemical equilibrium expectations. It is therefore necessary to connect the global equilibrium chemistry model to a model of the upper atmosphere in order to determine its observable atmospheric properties.

In order to determine the gas-phase chemistry throughout the atmosphere, we first break up the chemical species at the base of the atmosphere (i.e., the outputs of the H. E. Schlichting & E. D. Young 2022 chemical equilibrium model) into constituent elements. The elemental abundances are then used as an input to FASTCHEM COND (J. W. Stock et al. 2018, 2022; D. Kitzmann et al. 2025), a chemical equilibrium code that includes both equilibrium and rainout condensation. Equilibrium condensation treats condensation at each temperature and pressure point independently. However, this is not well suited to computing the composition of planetary atmospheres, since rainout will impact the distribution of elements available in the atmosphere as a function of altitude (A. Burrows & C. M. Sharp 1999).

In order to simulate the effect of rainout, FASTCHEM COND starts by calculating the chemistry at the highest pressure in the atmosphere and works its way toward lower pressures throughout a given pressure–temperature profile. Whenever condensation is encountered, the coupled condensation and gas-phase system is solved, yielding the effective elemental abundances of the condensing elements left in the gas phase (see Equation (12) in D. Kitzmann et al. 2025). These effective abundances are subsequently used to change the actual elemental abundances to the newly computed values at all pressures below the level at which condensation occurs. This impacts the abundances of elements remaining in the gas phase in the upper atmosphere, and can lead to a sudden decrease in the abundances of condensing elements. Calculation of the condensed phase requires temperature-dependent equilibrium constants, for which FASTCHEM COND uses a variety of data sources: R. Prydz & R. D. Goodwin (1972), L. Haar & J. S. Gallagher (1978), R. D. Goodwin (1985), C. M. Sharp & W. F. Huebner (1990), J. I. Moses et al. (1992), I. Barin (1995), M. Chase (1998), C. L. Yaws (1999), J. Dykyj et al. (2001), D. M. Murphy & T. Koop (2005), W. Wagner & H.-J. Kretzschmar (2008), D. Lide (2009), and H. P. Gail et al. (2013). Details regarding which sources are used for a given species can be found in Table A1 of D. Kitzmann et al. (2025).

We note that the H. E. Schlichting & E. D. Young (2022) model only includes the following elements: hydrogen, carbon, oxygen, iron, magnesium, silicon, and sodium. In general, we set the abundances of any other elements included in FASTCHEM COND to solar-composition values as described in M. Asplund et al. (2009), thereby assuming that the abundances of these elements are not affected by magma ocean interactions, a simplification that is necessary in order to couple the models. Other works have noted that nitrogen, which is not included in our magma–atmosphere interaction model, may be depleted relative to chemical equilibrium in the presence of a magma ocean (O. Shorttle et al. 2024). In order to test whether the lack of nitrogen chemistry in the H. E. Schlichting & E. D. Young (2022) impacts our results, we perform a sensitivity test by running models with a range of nitrogen abundances (see Section 3.5). As the goal of this project is to compare the abundances of molecules detected in the atmosphere of TOI-270 d (i.e., H_2O, CH_4, and CO_2) to the output of our model rather than to predict the abundances of nitrogen-bearing species, we include these models primarily as a check that the nitrogen depletion does not alter the compositions of the detected species nor introduce any additional detectable species. We discuss possible implications of the nondetections of nitrogen-bearing species in the atmosphere of TOI-270 d in further detail in Section 3.5.

2.3. Radiative–Convective Equilibrium

We model atmospheric temperature profiles and emission spectra using the one-dimensional radiative transfer code HELIOS (M. Malik et al. 2017, 2019a, 2019b). HELIOS computes atmospheric temperature profiles in radiative–convective equilibrium. In this work, we assume perfect heat redistribution between the planet's two hemispheres. To achieve this, we assume a heat redistribution factor of 0.25, which dilutes the incoming radiation in order to approximate the effect of averaging over the true nonuniform irradiation pattern (B. M. S. Hansen 2008). We include convective adjustment, with the adiabatic coefficient κ set to $2/7$, where $\kappa = (d \ln T / d \ln P)_S$. This is appropriate for an H_2-rich atmosphere in the absence of significant condensation.

Our model atmosphere extends from 10^{-6} to 10^3 bar. We note that this model is representative of the upper atmosphere alone, with the pressure at the base of the atmosphere being at much higher pressures than 10^3 bar. Indeed, the pressure at the base of the atmosphere depends on the redox state of the planet and therefore on the magma–atmosphere interaction itself (H. Nicholls et al. 2024). We adopt planetary parameters similar to those of TOI-270 d (V. Van Eylen et al. 2021; T. Mikal-Evans et al. 2023): $\log_{10} g_p$ (cgs) $= 2.96$, $a = 0.0733$ au, and $R_p = 2.19\, R_\oplus$. We simulate a stellar spectrum similar to TOI-270 by interpolating from a PHOENIX model grid (T. O. Husser et al. 2013), with $\log_{10} g_*$ (cgs) $= 4.872$, $T_{\rm eff} = 3506$ K, and [Fe/H] $= -0.2$ dex.

For a given composition, we generate opacity tables using the k-distribution method at a resolution $R = 300$ between 0.24 and 500 μm. We include opacity from the following species: C_2H_2 (K. L. Chubb et al. 2020), CH_4 (R. J. Hargreaves et al. 2020), CO and CO_2 (L. S. Rothman et al. 2010), H_2O (O. L. Polyansky et al. 2018), H_2S (A. A. A. Azzam et al. 2016; K. L. Chubb et al. 2018), HCN (R. J. Barber et al. 2014), NH_3 (P. A. Coles et al. 2019), O_2 (I. E. Gordon et al. 2022), PH_3 (C. Sousa-Silva et al. 2015), SiH_4 (A. Owens et al. 2017), SiO (E. J. Barton et al. 2013), and Fe, K, Mg, and Na (R. L. Kurucz & B. Bell 1995), as well as H_2–H_2 and H_2–He collision-induced absorption (CIA; C. Richard et al. 2012) and Rayleigh scattering. Each of these opacity sources covers a

wide temperature range, meaning no extrapolation is required to apply them in our model. Pressure broadening is applied following S. L. Grimm et al. (2021) to cover the full pressure range of the models.

The output of FASTCHEM COND is required to produce opacity tables which are input to HELIOS. However, it is not possible to account for rainout condensation without an initial HELIOS model to provide a pressure–temperature profile. We therefore initially assume equilibrium chemistry with no condensation across a wide range of temperatures (100–6000 K), which we input to HELIOS to produce an initial guess for the pressure–temperature profile. We then use this pressure–temperature profile as an input for FASTCHEM COND with rainout condensation included. This produces new chemical abundance profiles, which can then be returned to HELIOS. We iterate between the two models until the pressure–temperature profile converges. Our convergence criterion is that the difference between subsequent temperature profiles does not exceed 20 K in any layer of the atmosphere. Our initial HELIOS model without condensation uses a premixed opacity table. Subsequent iterations in which condensation is accounted for use on-the-fly opacity mixing using the random overlap resort–rebin method (D. S. Amundsen et al. 2017).

2.4. Photochemistry

Photochemical processes and vertical mixing also play a role in altering the chemical composition of the upper atmosphere. We account for these effects using the Photochem package (N. F. Wogan et al. 2023; N. Wogan 2024). Photochem is a chemical disequilibrium kinetics code which models the effects of thermochemistry, photolysis, and mixing, with elements inherited from K. Zahnle et al. (2016). We use the temperature profile and chemical abundances computed in previous steps as inputs to the photochemical model. Photochem performs calculations on an altitude grid that is initially derived initially from these inputs. Because disequilibrium chemistry and mixing introduce deviations in the mean molecular weight at each altitude grid point, Photochem continually alters and regrids the altitude–pressure profile such that the temperature profile is conserved (S. Mukherjee et al. 2025). We adopt the same planetary and stellar parameters as the previous modeling steps, apart from the stellar spectrum (see below). There is no strong evidence for hazes in the atmosphere of TOI-270 d, so we do not include aerosol particles in these models. We vary the strength of vertical mixing via the eddy diffusion coefficient K_{zz}, ranging from 10^3 to 10^9 cm^2 s^{-1} in steps of 1 dex. This range is chosen to follow previous studies of sub-Neptune photochemistry (e.g., S.-M. Tsai et al. 2021) while also allowing for lower values, which have been suggested for solar system giants (J. I. Moses et al. 2005).

It is important to use an appropriate stellar spectrum to ensure accurate photochemical modeling. Since a stellar spectrum of TOI-270 of sufficiently high quality is not available, we use the spectrum of GJ 832 as a proxy. GJ 832 has the same stellar type (M3V; J. S. Pineda et al. 2021) as TOI-270 (T. Mikal-Evans et al. 2023) and comparable effective temperature and surface gravity ($T_{\rm eff} = 3539^{+79}_{-74}$ K and $\log g$ (cgs) $= 4.792^{+0.036}_{-0.039}$ for GJ 832; $T_{\rm eff} = 3506 \pm 70$ K and $\log g = 4.872 \pm 0.026$ for TOI-270; J. S. Pineda et al. 2021; V. Van Eylen et al. 2021). The spectrum is acquired from the MUSCLES survey (K. France et al. 2016; R. O. P. Loyd et al. 2016; A. Youngblood et al. 2016).

2.5. Forward Model Spectra

Finally, we generate transmission spectra from the outputs of the previous modeling steps using AURA-3D (M. C. Nixon & N. Madhusudhan 2022). AURA-3D includes a radiative transfer scheme that allows for the generation of spectra with thermal and chemical profiles that vary with height, longitude, and latitude in the atmosphere. It is built on the AURA family of retrieval codes (A. Pinhas et al. 2018; M. C. Nixon & N. Madhusudhan 2020), with the version used in this project also incorporating developments presented in L. Welbanks & N. Madhusudhan (2021) and M. C. Nixon et al. (2024a). Although AURA-3D can generate models with three-dimensional geometry, the temperature and abundance profiles vary with height only in this work, since the outputs of HELIOS and Photochem only depend on height (i.e., pressure).

AURA-3D is used to compute the transmission spectrum for a transiting planet, accounting for opacity contributions from chemical species, CIA, and clouds or hazes. We use the same line lists as described in Section 2.3, and use opacity sampling at $R = 60{,}000$ to generate forward models. Volume mixing ratios and pressure–temperature profiles are taken directly from the output of Photochem and HELIOS, respectively. We note that some gases (e.g., N_2) included in the Photochem output are not spectrally active, so their opacities are not included in the forward model. However, their volume mixing ratios are still accounted for in order to calculate the atmospheric mean molecular weight, which plays a role in determining the amplitude of atmospheric features in the transmission spectrum. In keeping with other components of our modeling framework, we adopt planetary parameters of TOI-270 d and stellar parameters of TOI-270 from V. Van Eylen et al. (2021) and T. Mikal-Evans et al. (2023).

3. Results

In this section we describe the vertical atmospheric temperature profiles and compositions that are produced by our modeling framework, and compare our results to the retrieved atmospheric composition of TOI-270 d found by B. Benneke et al. (2024).

3.1. Temperature Profiles

Figure 2 shows converged atmospheric temperature profiles from HELIOS for the range of model parameters considered. All temperature profiles converged within two iterations between HELIOS and FASTCHEM COND, although there were some more significant deviations ($\Delta T > 150$ K) between the initial temperature profile without condensation and the first temperature profile calculated once condensation had been accounted for. Overall, there is not significant variation in the converged temperature profiles for different scenarios. We find that higher core–mantle and mantle–atmosphere boundary temperatures lead to hotter temperatures in the deep atmosphere. Models with higher iron mass fractions also have hotter temperature profiles, although the effect becomes less pronounced for models with hotter boundary temperatures. The difference is most notable at pressures higher than 1 bar. This is likely a result of models with hotter boundary temperatures having higher atmospheric metallicity, including higher H_2O and CH_4 abundances (see Figure 4). Higher H_2O and CH_4 abundances cause the atmosphere to be optically thick at lower pressures, which results in higher temperatures

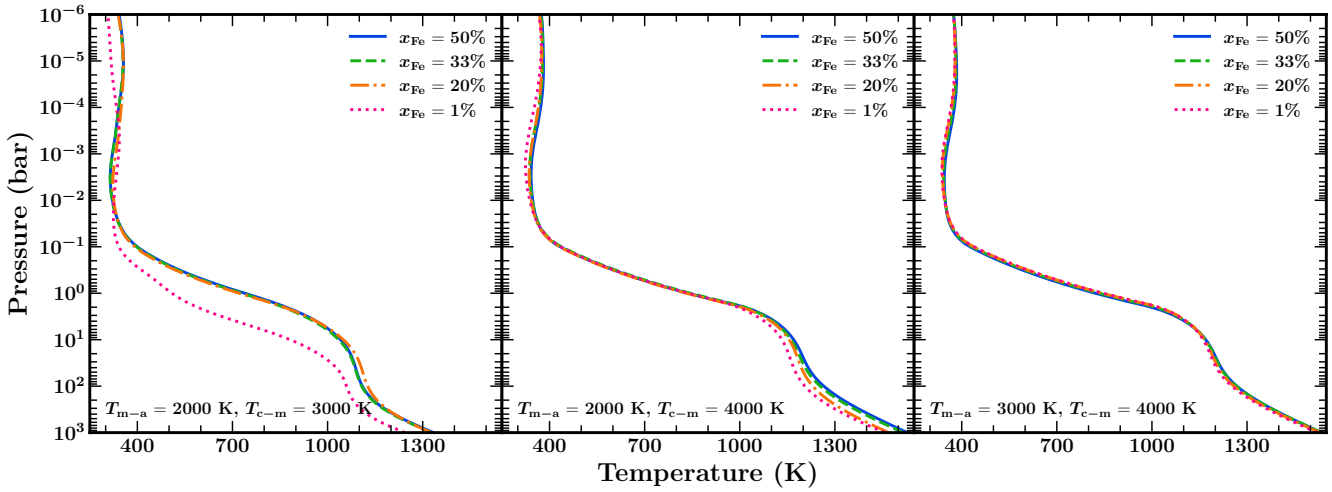

Figure 2. Temperature profiles for TOI-270 d from HELIOS. Each panel shows a different combination of core–mantle and mantle–atmosphere boundary temperatures. The different colors and line styles for each profile represent different iron mass fractions, shown as a percentage of the mass of the nucleus of the planet (i.e., the iron and silicate components).

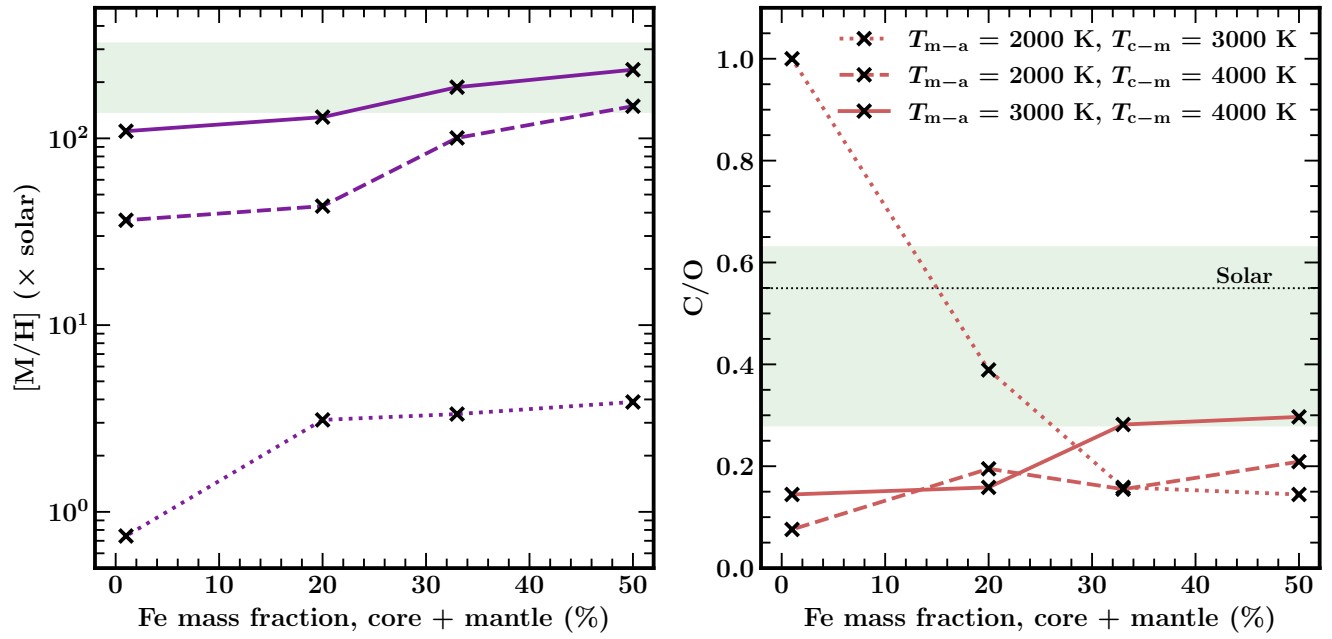

Figure 3. Metallicity ([M/H], left) and C/O ratio (right) of the upper atmosphere of TOI-270 d (P = 1 mbar) for different magma ocean model scenarios. [M/H] and C/O are plotted as a function of the iron mass fraction, shown as a percentage of the total mass of the nucleus (core + mantle). The metallicity [M/H] is calculated as [(C + O)/H] relative to solar abundances (M. Asplund et al. 2009), since carbon- and oxygen-bearing species are the main drivers of the metallicity constraints presented in B. Benneke et al. (2024). Different line styles represent different combinations of mantle–atmosphere and core–mantle boundary temperatures (T_{m-a} and T_{c-m}, respectively). The green shaded regions show the constraints on [M/H] and C/O reported by B. Benneke et al. (2024), inferred from the JWST transmission spectrum of the planet. The black dotted line in the right-hand panel shows the solar C/O value from M. Asplund et al. (2009).

in the deep atmosphere due to a stronger greenhouse effect (e.g., E. M. R. Kempton et al. 2023a). We note that the mantle–atmosphere boundary temperature is not equivalent to the temperature at 10^3 bar—the mantle–atmosphere boundary is found at higher pressures than those modeled by HELIOS.

3.2. Atmospheric Metallicity and C/O

We begin our exploration of the resulting atmospheric chemistry by investigating the metallicity and C/O of the upper atmosphere (P = 1 mbar), as depicted in Figure 3. Since the metallicity constraint for TOI-270 d is derived from the volume mixing ratios of carbon- and oxygen-bearing species, we use [(C + O)/H] as a proxy for metallicity. For most of the models considered in this work, magma ocean interactions lead to an atmospheric metallicity that is enhanced relative to solar, and a C/O that is depleted relative to solar. This qualitatively agrees with previous work exploring magma–atmosphere interactions (e.g., C. Seo et al. 2024; A. Werlen et al. 2025). The extent of these changes to metallicity and C/O depend on the thermodynamic conditions at the atmosphere–mantle and mantle–core boundaries, as well as the iron mass fraction in the nucleus of the planet. The atmospheric metallicity increases as the boundary temperatures increase, and also increases as the iron mass fraction increases. One of the most important reaction pathways leading to the formation of water requires participation of

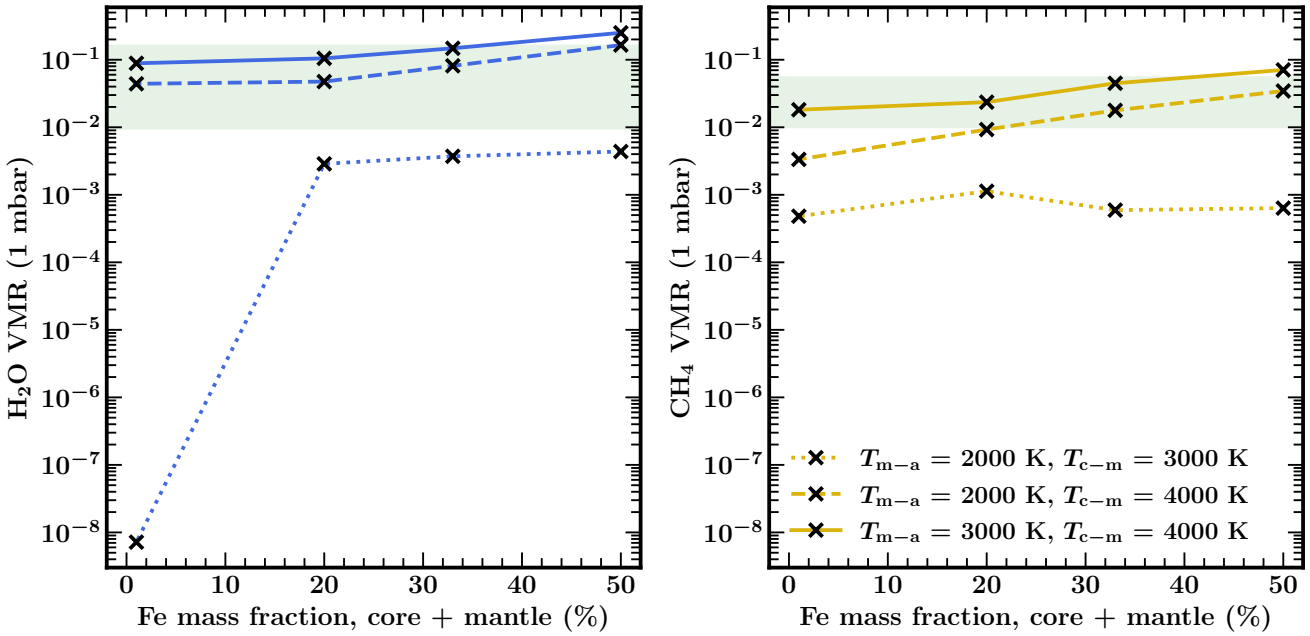

Figure 4. Volume mixing ratio of H_2O (left) and CH_4 (right) in the upper atmosphere of TOI-270 d ($P = 1$ mbar) for different magma ocean model scenarios. We show models with $K_{zz} = 10^7$ cm^2 s^{-1}, although the differences in the H_2O and CH_4 volume mixing ratios are negligible for different values of K_{zz}. Volume mixing ratios are plotted as a function of the iron mass fraction, shown as a percentage of the total mass of the nucleus (core + mantle). Different line styles represent different combinations of mantle–atmosphere and core–mantle boundary temperatures (T_{m-a} and T_{c-m}, respectively). The green shaded regions show the constraints on the volume mixing ratios of H_2O and CH_4 reported by B. Benneke et al. (2024), inferred from the JWST transmission spectrum of the planet.

elements found in the iron-rich core (E. S. Kite et al. 2020; H. E. Schlichting & E. D. Young 2022), which explains why metallicity decreases when the core mass fraction decreases.

A notable exception to the overall finding that metallicity is enhanced and C/O is depleted is the case where $T_{m-a} = 2000$ K, $T_{c-m} = 3000$ K, and $x_{Fe} = 1\%$. For these parameters, the atmospheric metallicity becomes slightly subsolar, and the C/O is enhanced to $\sim$1. These effects are explained in part due to the low iron mass fraction, as described above, and also as a result of the cooler temperature profile for this model, which leads to H_2O condensation (see Section 3.3). A low atmospheric metallicity could therefore be the result of an interior with very little chemically reactive iron. However, it is unclear how such an iron-poor planet would form (L. A. Rogers 2015). Additionally, flotation or suspension of metal droplets in the convective magma ocean have been suggested to increase the mass of chemically reactive iron in the magma oceans of sub-Neptunes (T. Lichtenberg 2021; E. D. Young et al. 2024). We further note that in this case, the assumption that the adiabatic index $\kappa = 2/7$ may no longer be appropriate, due to the role of condensation. We reserve further examination of the impact of H_2O condensation on these models for a future study, since there is no evidence for H_2O depletion in the upper atmosphere of TOI-270 d.

The green shaded regions in Figure 3 show the retrieved metallicity and C/O of the atmosphere of TOI-270 d from B. Benneke et al. (2024). The retrieved atmospheric metallicity from that work is $225^{+98}_{-86} \times$ solar, and the retrieved C/O is $0.47^{+0.16}_{-0.19}$. We find that two of our models are consistent with both values to within 1σ. This is achieved when $T_{m-a} = 3000$ K, $T_{c-m} = 4000$ K, and $x_{Fe} = 33\%$ or 50%. This suggests that magma–atmosphere interactions may be able to explain the observed atmosphere of the planet. Our next step is to move beyond atmospheric metallicity and C/O, and compare the abundances of specific chemical species that were detected in the planet's atmosphere (B. Benneke et al. 2024) to the outputs of our model.

3.3. Molecular Volume Mixing Ratios

The resulting volume mixing ratios of H_2O and CH_4 at 1 mbar are shown in Figure 4. Similarly to the atmospheric metallicity, we find that H_2O and CH_4 are enhanced relative to solar composition for both scenarios in which $T_{c-m} = 4000$ K (where solar $\log_{10} X_{H_2O} = -3.0$ and $\log_{10} X_{CH_4} = -3.3$; e.g., J. I. Moses et al. 2013). This enhancement increases further as T_{m-a} rises. When $T_{c-m} = 3000$ K, the H_2O volume mixing ratio is only slightly to increased relative solar composition, while the CH_4 volume mixing ratio remains approximately solar. As seen in Figure 3, the model with the lowest iron mass fraction is an outlier, with the H_2O volume mixing ratio depleted due to condensation.

We find that numerous combinations of model parameters can explain the retrieved H_2O and CH_4 volume mixing ratios for TOI-270 d. B. Benneke et al. (2024) report $\log_{10} X_{H_2O} = -1.10^{+0.31}_{-0.92}$ and $\log_{10} X_{CH_4} = -1.64^{+0.38}_{-0.36}$. Seven of the 12 models shown in Figure 4 yield H_2O volume mixing ratios that are consistent with the retrieved H_2O, and five yield CH_4 volume mixing ratios that are consistent with the retrieved CH_4. This indicates that a magma–atmosphere interaction model can readily reproduce these volume mixing ratios.

We find that the volume mixing ratios of H_2O and CH_4 are largely unaffected by vertical mixing and photochemistry. For this reason, Figure 4 only shows results for $K_{zz} = 10^7$ cm^2 s^{-1}, with other values yielding essentially the same values. The same cannot be said for the volume mixing ratios of CO and CO_2. Without considering vertical mixing, the volume mixing ratios of CO and CO_2 sharply decrease at $P \lesssim 1$ bar, which is inconsistent with the detection of CO_2 reported by B. Benneke et al. (2024).

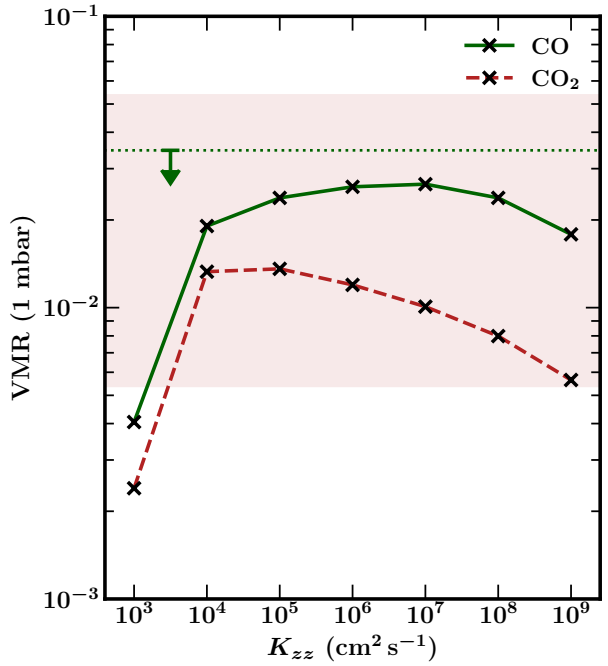

Figure 5. Volume mixing ratios of CO (green, solid) and CO_2 (red, dashed) in the upper atmosphere of TOI-270 d (P = 1 mbar) as a function of K_{zz}. T_{m-a} = 3000 K, T_{c-m} = 4000 K, and x_{Fe} = 33% for all models shown here. The red shaded region shows the constraints on the volume mixing ratio of CO_2 reported by B. Benneke et al. (2024), and the green dotted line shows the reported 2σ upper limit for CO.

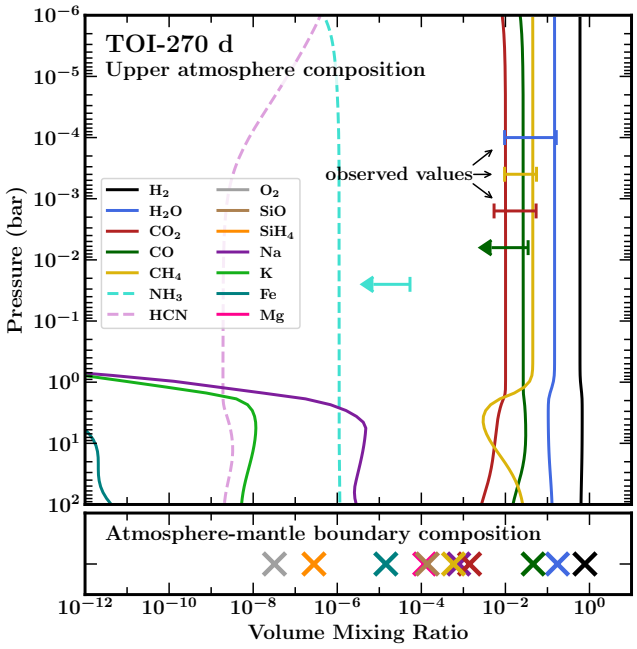

Figure 6. Volume mixing ratio profiles for chemical species in the atmosphere of TOI-270 d, based on interactions between a magma ocean and a gaseous atmosphere with an initial solar composition. Model parameters are T_{m-a} = 3000 K, T_{c-m} = 4000 K, x_{Fe} = 33%, and K_{zz} = 10^7 cm^2 s^{-1}. The bottom panel shows volume mixing ratios of species at the mantle–atmosphere interface ($P \gg 100$ bar). Error bars and arrows show measured volume mixing ratios or upper limits for H_2O; CH_4 and CO_2; and CO and NH_3 in the upper atmosphere, derived from JWST observations of TOI-270 d (B. Benneke et al. 2024). Dashed lines show nitrogen-bearing chemical species not included in the magma ocean model, but included in the upper atmosphere model. In the case shown here, atmospheric nitrogen is depleted to $10^{-2}\times$ solar.

However, vertical mixing serves to enhance the upper atmospheric concentrations of these molecules considerably, a phenomenon which has been reported in models of other planets (e.g., WASP-107 b; L. Welbanks et al. 2024).

Figure 5 compares the volume mixing ratios of CO and CO_2 at 1 mbar for models with $T_{m-a} = 3000$ K, $T_{c-m} = 4000$ K, and $x_{Fe} = 33\%$ across the range of values of K_{zz} considered in our photochemical model. We choose to highlight this set of parameters since they yield values of [M/H], C/O, X_{H_2O}, and X_{CH_4} that are consistent with atmospheric observations of TOI-270 d. The CO and CO_2 concentrations above the quench pressure are homogenized to their values at the quench pressure by vertical mixing. As K_{zz} increases, the quench pressure moves deeper in the atmosphere, and the volume mixing ratios change accordingly. We find that for $K_{zz} \geqslant 10^4$ cm^2 s^{-1}, the volume mixing ratio of CO_2 is consistent with the retrieved $\log_{10} X_{CO_2} = -1.67^{+0.40}_{-0.60}$ from B. Benneke et al. (2024). We find that the volume mixing ratio of CO is also enhanced, but remains below the 2σ upper limit reported in that work ($\log_{10} X_{CO} < -1.46$). Such an increase of CO over CO_2 is consistent with O. Shorttle et al. (2024) and H. Nicholls et al. (2024), who identified increasing atmospheric CO for intermediate magma ocean redox states as an important tracer of interaction with the interior.

The bottom panel of Figure 6 shows the volume mixing ratios of species at the atmosphere–mantle boundary, i.e., the output of the H. E. Schlichting & E. D. Young (2022) model. We note that several species appear at the atmosphere–mantle boundary which are not present in the upper atmosphere, including the silicon-bearing species SiO and SiH_4. These species have previously been highlighted as possible signatures of atmosphere–interior interactions (e.g., W. Misener et al. 2023). However, we do not expect these species to be present in the upper atmosphere of TOI-270 d due to condensation. We confirm this by comparing our final model to our initial model that does not account for condensation, and find that in the case without condensation, SiO and SiH_4 are present in appreciable quantities, similar to their volume mixing ratios at the atmosphere–mantle boundary. This suggests that for hotter planets, SiO and SiH_4 could indeed be present and used to infer atmosphere–interior interactions, although a detailed investigation is beyond the scope of this work.

In order to test whether the uncertainty in the total iron and silicate budget of our planet impacts our results, we include two additional model cases with the total iron and silicate mass set to 3.8 $M_\oplus$ and 4.8 $M_\oplus$, spanning the reported 1σ range from B. Benneke et al. (2024). For these models we fix $T_{m-a} = 3000$ K, $T_{c-m} = 4000$ K, $x_{Fe} = 33\%$, and $K_{zz} = 10^7$ cm^2 s^{-1}. We find that the upper atmospheric concentrations of H_2O, CH_4, CO, and CO_2 deviate slightly from their values in the 4.3 $M_\oplus$ model, but by less than 0.04 dex in all cases, much smaller than the reported uncertainties on measurements from JWST. We therefore conclude that the uncertainty in the iron and silicate mass does not alter our overall findings.

3.4. Comparison with JWST Observations

We find that a subset of our models is able to match the retrieved atmospheric abundances for TOI-270 d reported in B. Benneke et al. (2024). Figure 6 shows the volume mixing ratios of key chemical species as a function of pressure in the case where $T_{m-a} = 3000$ K, $T_{c-m} = 4000$ K, $x_{Fe} = 33\%$, and $K_{zz} = 10^7$ cm^2 s^{-1}. We find that all of the major carbon- and

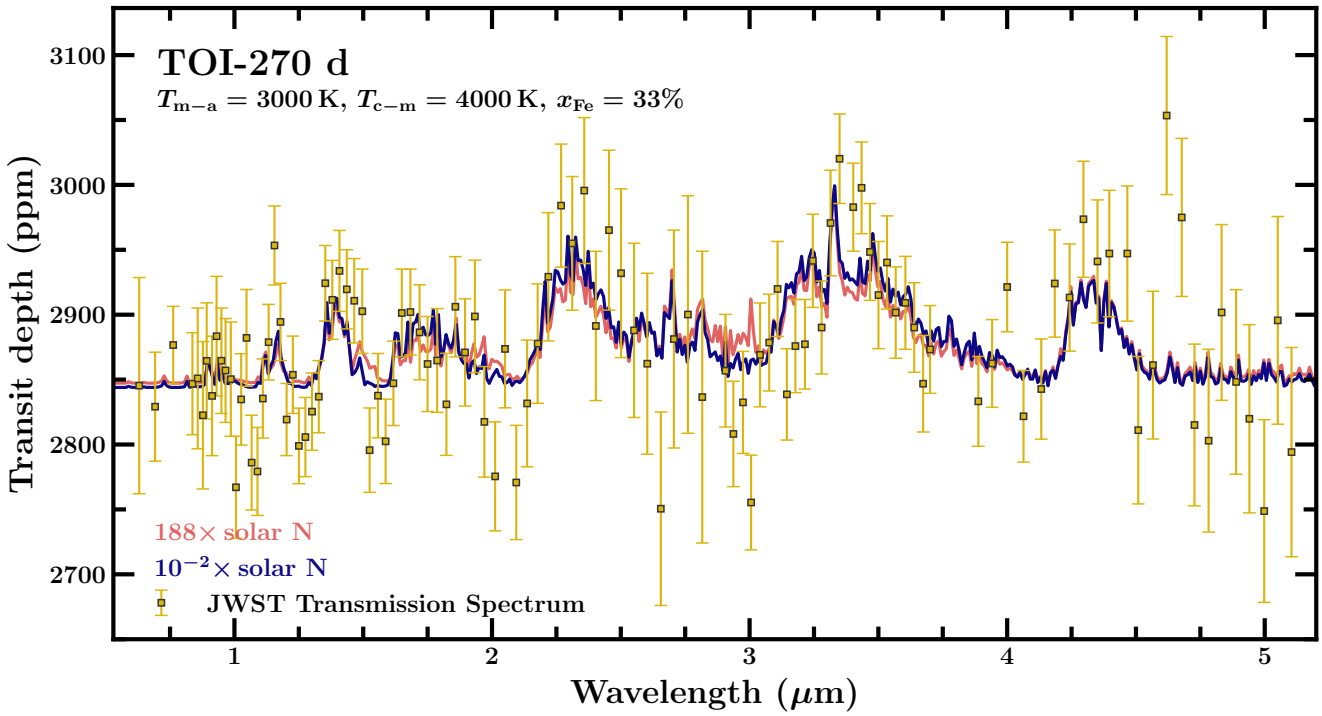

Figure 7. Transmission spectrum of TOI-270 d. Gold squares with error bars show the observed JWST spectrum from B. Benneke et al. (2024). The pink and blue lines show forward modeled spectra assuming the upper atmospheric composition from our coupled magma–atmosphere model. Model parameters are $T_{m-a} = 3000$ K, $T_{c-m} = 4000$ K, $x_{Fe} = 33\%$, and $K_{zz} = 10^7$ cm^2 s^{-1}. The pink line shows a case where nitrogen is enhanced in line with the carbon and oxygen enhancement found by the magma–atmosphere model. The blue line shows a case where nitrogen is depleted to 10^{-2} × solar abundance, in line with expectations of nitrogen depletion from magma–atmosphere interactions (O. Shorttle et al. 2024). For the model with enhanced nitrogen, $\chi^2/n_{data} = 1.31$, and for the model with depleted nitrogen, $\chi^2/n_{data} = 1.18$.

oxygen-bearing species are consistent within the 1σ retrieved abundances for species which were detected in the atmosphere (i.e., H_2O, CH_4, and CO_2), or below the reported upper limit in the case that the species was not detected (i.e., CO).

We further demonstrate the capability of our model to explain JWST observations of TOI-270 d by generating a forward model transmission spectrum for direct comparison to the data. We use the temperature profile and chemical abundances from our model with $T_{m-a} = 3000$ K, $T_{c-m} = 4000$ K, $x_{Fe} = 33\%$, and $K_{zz} = 10^7$ cm^2 s^{-1}. Additionally, we varied the nitrogen abundance to account for its possible depletion (see Section 3.5). Two more parameters are required to produce a forward model spectrum: a reference pressure P_{ref} and cloud deck pressure P_{cloud}. P_{ref} is the pressure assigned to the white-light radius of the planet and has the effect of changing the transit depth by a constant value across all wavelengths, whereas P_{cloud} reduces the size of atmospheric spectral features by setting the optical depth to ∞ for $P > P_{cloud}$. B. Benneke et al. (2024) reported a lower limit on P_{cloud} of $10^{-2.99}$ bar, and did not report constraints on P_{ref}. We therefore generated a grid of models with $P_{cloud} > 10^{-2.99}$ bar and P_{ref} within the full range of pressures from the chemistry models, with a step size of 0.5 dex. This allowed us to find a best-fit spectrum given our chosen chemistry and temperature profiles by selecting the model that resulted in the lowest χ^2/n_{data}. When fitting the NIRISS/SOSS and NIRSpec G395H data, we assumed an offset of 12 ppm between the spectra of each instrument, according to the offset reported by B. Benneke et al. (2024).

Our resulting spectra are shown in Figure 7. Our optimal parameter values were $P_{ref} = 1$ bar and $P_{cloud} = 10^{-2.5}$ bar. This parameter combination yielded $\chi^2/n_{data} = 1.18$ for the model with nitrogen depleted to 10^{-2} × solar. For this data set, we can approximate the standard deviation of χ^2/n_ν to be 0.13, following R. Andrae et al. (2010). This indicates that models with $0.74 \leqslant \chi^2/n_\nu \leqslant 1.26$ are consistent with the data at the 2σ level. The value of χ^2/n_ν is likely somewhat higher than our calculated $\chi^2/n_{data} = 1.18$, though it is difficult to estimate the number of degrees of freedom, n_ν, for a nonlinear model. Nevertheless, these calculations suggest that the model agrees with the data at the $<2\sigma$ level. We deem this to be a good level of agreement, particularly given that this is a self-consistent forward model rather than a retrieval result from a full exploration of parameter space. We note that spectra with $1 \times$ solar and $10^{-4} \times$ solar nitrogen abundances are almost indistinguishable from the $10^{-2} \times$ solar case. We discuss the scenario with enhanced nitrogen relative to solar values in Section 3.5.

M. Holmberg & N. Madhusudhan (2024) also presented an analysis of the Hubble Space Telescope (HST)/WFC3 + NIRSpec G395H transmission spectrum of TOI-270 d. That study reported a range of abundance constraints depending on factors such as the treatment of limb darkening. A number of our models with lower iron mass fractions and/or $T_{c-m} = 3000$ K come close to matching their reported abundances. For example, the "one offset + constant limb darkening" analysis presented by M. Holmberg & N. Madhusudhan (2024) reports the following abundances: $\log_{10} X_{H_2O} = -1.04^{+0.24}_{-0.45}$, $\log_{10} X_{CH_4} = -2.97^{+0.30}_{-0.39}$, $\log_{10} X_{CO_2} = -3.95^{+0.72}_{-0.90}$, and $\log_{10} X_{CO} < -3.37$ (95% upper limit). By comparison, our model where $T_{m-a} = 2000$ K, $T_{c-m} = 4000$ K, $x_{Fe} = 1\%$, and $K_{zz} = 10^6$ cm^2 s^{-1} has $\log_{10} X_{H_2O} = -1.36$, $\log_{10} X_{CH_4} = -2.48$, $\log_{10} X_{CO_2} = -4.73$, and $\log_{10} X_{CO} = -3.87$. Each of these volume mixing ratios agree with the measured values, with the exception of CH_4, which we

find to have a slightly higher concentration than the 1σ range reported by M. Holmberg & N. Madhusudhan (2024). We discuss this finding in more detail in Section 4.1.

3.5. Impact of Nitrogen Depletion

Since the model used to calculate chemical equilibrium abundances between the core, mantle, and atmosphere does not include nitrogen- or sulfur-bearing species, our work primarily focuses on determining the abundances of carbon- and oxygen-bearing species that were detected in the atmosphere of TOI-270 d. However, O. Shorttle et al. (2024) demonstrated that magma–atmosphere interactions could lead to depleted atmospheric nitrogen, impacting the abundances of species such as NH_3. Although we leave the full incorporation of nitrogen chemistry into our model for a further study, we conduct a sensitivity test to determine whether the abundances of other atmospheric species are impacted by varying the atmospheric nitrogen abundances. We also explore the extent to which the upper limit for NH_3 reported by B. Benneke et al. (2024) can inform us as to whether nitrogen is depleted in the atmosphere of TOI-270 d.

For our sensitivity test, we focus on models where $T_{m-a} = 3000$ K, $T_{c-m} = 4000$ K, and $x_{Fe} = 33\%$. These parameters are chosen since they provide the best overall explanation for the observed atmosphere of TOI-270 d. For the photochemistry and vertical mixing, we include the full range of K_{zz} values included in our previous model grid. We wish to determine whether varying the nitrogen abundance leads to changes in the volume mixing ratios of the three chemical species that were detected in the atmosphere of TOI-270 d: H_2O, CH_4, and CO_2. Additionally, we compare the CO volume mixing ratio to its measured upper limit. We consider four different values for the nitrogen abundance by volume: $188\times$ solar, $1\times$ solar, $10^{-2}\times$ solar, and $10^{-4}\times$ solar. Our maximum value is chosen to match the atmospheric metallicity $[(C+O)/H]$ of the magma–atmosphere model. We include a $1\times$ solar case to represent a scenario in which nitrogen is unaffected by magma–atmosphere interactions. The remaining two cases reflect scenarios in which nitrogen is depleted from the atmosphere, with values spanning the range presented by O. Shorttle et al. (2024).

For the $1\times$ solar, $10^{-2}\times$ solar and $10^{-4}\times$ solar cases, we find that changes in the abundances of H_2O, CH_4, CO, and CO_2 are negligible. Across all chemical species and K_{zz} values, the maximum fractional change in abundance at 1 mbar is $\Delta X_i/X_i = 6.4\times10^{-4}$. We therefore conclude that our results are not sensitive to possible depletion of nitrogen in the atmosphere. However, we do find that the abundances of these species change when we allow for nitrogen to be enhanced to the metallicity indicated by the C and O abundances. In this case, we see an increase in the H_2O volume mixing ratio and a decrease in CH_4, CO, and CO_2. For example, when $K_{zz} = 10^7$ cm^2 s^{-1}, the volume mixing ratios of CH_4, CO, and CO_2 decrease by a factor of 2.35, 1.73, and 1.36, respectively, in the enhanced nitrogen model. For these species, the depleted values are still consistent with the abundance estimates from B. Benneke et al. (2024). However, the H_2O volume mixing ratio increases from 14.8% in the solar nitrogen case to 18.1% in the enhanced nitrogen case, making it slightly higher than the 1σ upper limit of 16.2% reported by B. Benneke et al. (2024). This suggests that an atmosphere uniformly enhanced in metals relative to hydrogen may be unlikely for the target, potentially lending further evidence that its atmosphere has been affected by magma ocean interactions, although we note that the change in goodness of fit to observations between these models is quite small (see Figure 7 and Section 4.2).

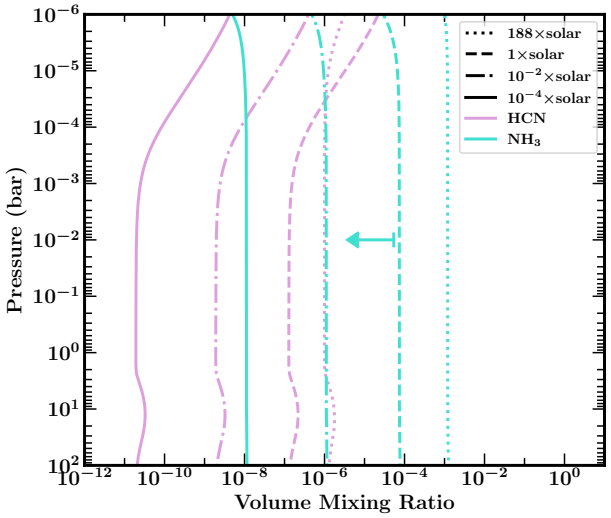

Figure 8. Volume mixing ratio profiles for NH_3 and HCN for a range of initial atmospheric nitrogen abundances. Model parameters are $T_{m-a} = 3000$ K, $T_{c-m} = 4000$ K, $x_{Fe} = 33\%$, and $K_{zz} = 10^7$ cm^2 s^{-1}. The $188\times$ solar case represents nitrogen enhancement in line with the derived metallicity from the resulting carbon and oxygen abundances from the magma–atmosphere model. The arrow represents the 2σ upper limit for the NH_3 volume mixing ratio according to B. Benneke et al. (2024).

We also explored how varying the total nitrogen budget for the atmosphere impacts the presence of key nitrogen-bearing species in the atmosphere, namely NH_3 and HCN. The volume mixing ratios of these two species for different levels of nitrogen enhancement are shown in Figure 8. We focus on models where $K_{zz} = 10^7$ cm^2 s^{-1}, as the volume mixing ratios of other species are consistent with observations in this case (see Figure 6). This figure demonstrates how the NH_3 abundance decreases as the total amount of nitrogen in the atmosphere decreases. We find that models assuming $10^{-2}\times$ solar and $10^{-4}\times$ solar nitrogen abundances are consistent with the upper limits for NH_3 presented by B. Benneke et al. (2024), whereas the $188\times$ solar and $1\times$ solar models exceed this upper limit, albeit only slightly for the $1\times$ solar case. This implies that nitrogen is likely to be depleted in this atmosphere, which is qualitatively consistent with magma ocean interactions according to O. Shorttle et al. (2024). However, we note that detecting and constraining the abundance of NH_3 is challenging for this target (see Section 4.2 for further details).

4. Discussion and Conclusions

4.1. Does TOI-270 d Require a Magma Ocean to Explain Its Observed Atmosphere?

Our findings suggest that the observed chemical abundances in the atmosphere of TOI-270 d can be readily explained as the outcome of interactions between an initially H_2-dominated atmosphere and an underlying magma ocean. This suggests that the planet need not have formed beyond the snowline, where accretion of icy material is more prevalent, to explain its high atmospheric metallicity and water content. However, while magma–atmosphere interactions may be sufficient to

explain the observed atmosphere, it is not yet possible to claim that they are necessary. Indeed, accretion of ices at formation is still a possible cause of this planet's atmospheric composition. Further work will be required to distinguish between different formation and evolutionary scenarios. In particular, assessing the outcome of interactions between a hydrogen atmosphere and a mixed rock + ice layer would be an interesting avenue for further study. However, even after accounting for different compositions of the core and mantle, evolutionary processes such as photoevaporative atmospheric escape and core-powered mass loss could further alter the atmospheric composition (M. Schulik & R. A. Booth 2023; C. Cherubim et al. 2025; K. Heng et al. 2025) over similar or longer timescales compared to magma–atmosphere interactions. In order to truly assess the prevalence of magma ocean interactions on sub-Neptunes, a more complete evolutionary model is required. However, we believe that this work, alongside similar studies (O. Shorttle et al. 2024; H. Nicholls et al. 2025), highlights that developing an understanding of how magma oceans shape sub-Neptune atmospheres will be critical as we strive to better understand the origins and nature of these objects.

In contrast to B. Benneke et al. (2024), who suggest that their findings are consistent with TOI-270 d hosting a mixed supercritical atmosphere atop an iron + rock nucleus, M. Holmberg & N. Madhusudhan (2024) argue that the atmosphere of TOI-270 d is consistent with the planet hosting a liquid water ocean, citing detections of CO_2 and CH_4 alongside a nondetection of NH_3 as evidence for this scenario. Our work demonstrates that detectable levels of CO_2 and CH_4 can be present in the upper atmosphere as a result of magma–atmosphere interactions and vertical mixing. Similar results have been obtained for the cooler sub-Neptune K2-18 b, another planet with claims of atmospheric CO_2 and CH_4 (N. Madhusudhan et al. 2023). Both a liquid water ocean (N. Madhusudhan et al. 2023) and a combination of magma–atmosphere interactions and vertical mixing (O. Shorttle et al. 2024; N. F. Wogan et al. 2024) have been suggested to explain this composition. The qualitative agreement between the compositions predicted by both scenarios suggests that additional work is required to find unique chemical signatures of both magma–atmosphere interactions and liquid water oceans.

Our model grid includes several cases which closely match the abundance constraints from B. Benneke et al. (2024). While some of our models also find relatively good agreement with the abundance constraints from M. Holmberg & N. Madhusudhan (2024), those models typically have lower iron mass fractions and core–mantle interface temperatures. However, we do not believe that the M. Holmberg & N. Madhusudhan (2024) results therefore indicate a true preference for a silicate-rich and/or cooler interior. In this work we did not conduct a detailed sampling of the parameter space, instead generating models with a smaller set of reasonable parameter values. It is therefore possible that some additional unexplored combination of parameters may explain the M. Holmberg & N. Madhusudhan (2024) results without a low $x_{\rm Fe}$ or $T_{\rm c-m}$. Furthermore, our models are physically and chemically consistent, rather than assuming that all individual abundances are free parameters, as is the case for the B. Benneke et al. (2024) and M. Holmberg & N. Madhusudhan (2024) analyses. This means that individual molecular abundances cannot be fine-tuned in order to improve the quality of fit to the spectrum. We also note that the two papers consider different sets of observations: B. Benneke et al. (2024) fit models to the JWST NIRISS + NIRSpec transmission spectrum of the planet, whereas M. Holmberg & N. Madhusudhan (2024) use the HST/WFC3 spectrum alongside JWST NIRSpec. Overall, the general agreement between the predicted and measured abundances, as well as the low-χ^2 values obtained when comparing our models to the JWST spectrum (Figure 7) indicate that our models are not ruled out by the present JWST observations.

Our models typically find that CO is more abundant in the upper atmosphere than CO_2 (see Figure 5), in agreement with previous studies considering magma–atmosphere interactions at low to moderate redox states (H. Nicholls et al. 2024; O. Shorttle et al. 2024). Although CO_2 has been identified in the atmosphere of TOI-270 d, while CO has not, the predicted CO abundances from our models remain below the upper limit suggested by B. Benneke et al. (2024). Additional observations to refine the CO abundance measurement may be useful to identify evidence for magma–atmosphere interactions.

4.2. Detectability of Ammonia on Sub-Neptunes

Figure 7 shows model transmission spectra for cases in which the atmospheric nitrogen abundance differs by over 4 orders of magnitude. Despite this, the change in transit depth is relatively small: the difference in $\chi^2/n_{\rm data}$ is just 0.13 between the two models, suggesting they are consistent with each other within $\sim 1\sigma$. This highlights that the detection of nitrogen-bearing species such as NH_3 on sub-Neptunes will be challenging. Due to its relatively minor impact on the transmission spectrum, the nondetection of NH_3 in the atmosphere of this planet from extant transmission spectroscopy does not necessarily imply its absence. Optimal strategies for detecting NH_3 may involve stacking multiple transits centered on the 2.9–3.1 μm region, where its absorption is most prominent, as well as acquiring transmission spectra with MIRI Low Resolution Spectroscopy to cover the NH_3 feature from 10.3–11 μm (see e.g., L. Welbanks et al. 2024). Given the apparent diagnostic power of nitrogen-bearing species for sub-Neptunes, it may be worth investing significant observing time in order to acquire robust detections and abundance measurements.

4.3. Additional Parameters of Interest

The goal of this study was to determine whether magma–atmosphere interactions are sufficient to explain recent JWST observations of the sub-Neptune TOI-270 d. For this reason, we chose to fix the majority of model parameters to nominal values, only varying a small number of parameters of interest. Constructing models with these nominal parameters was sufficient to demonstrate that interactions with a magma ocean can indeed produce atmospheres for TOI-270 d that are consistent with the composition derived by B. Benneke et al. (2024) from its JWST transmission spectrum. However, we note that it may be of interest in a future study to assess how varying some of these parameters could influence the resulting upper atmospheric compositions. For example, H. E. Schlichting & E. D. Young (2022) noted that the total atmospheric mass fraction of the initial planet (before interacting with the core and mantle) could affect the final atmospheric composition, with

larger initial atmospheres leading to higher abundances of H_2 and lower abundances of other chemical species. For this work, we chose an initial atmospheric mass fraction of 1.5%, which is consistent with internal structure models of the planet assuming an H_2-dominated atmosphere (V. Van Eylen et al. 2021). In reality, magma–atmosphere interactions likely take place while the planet is still accreting its atmosphere and chemically differentiating internally. Developing a complete model of these interactions would require simultaneously allowing for the influx of new gaseous material as it accretes onto the planet, while allowing the existing atmosphere to react with the core and mantle. Such a model is beyond the scope of this study. We note that H. E. Schlichting & E. D. Young (2022) found that increasing the total atmospheric mass fraction led to a slight increase in the final H_2 abundance relative to other chemical species (i.e., lower atmospheric metallicity), but that this effect was less pronounced than that of varying the interface temperatures.

We also assumed core and mantle compositions following H. E. Schlichting & E. D. Young (2022). The chosen composition results in an oxygen fugacity relative to the iron–wüstite buffer $\Delta\mathrm{IW} = -2.8$, where $\Delta\mathrm{IW}$ is defined in Equation (12) of H. E. Schlichting & E. D. Young (2022). A number of studies have demonstrated that varying the oxygen fugacity can alter the atmospheric composition (e.g., F. Gaillard et al. 2022; H. Nicholls et al. 2024, 2025; F. E. Rigby et al. 2024; O. Shorttle et al. 2024). Although exploring the effect of oxygen fugacity was not required in this study to show that it is possible for our model to explain the observed atmosphere of TOI-270 d, more extensive theoretical work could eventually allow for upper atmospheric composition to be used as a tracer of oxygen fugacity in exoplanetary interiors (T. Lichtenberg & Y. Miguel 2025).

4.4. Model Limitations and Caveats

In addition to the need to couple interactions between the core, mantle, and atmosphere to evolutionary models as discussed above, H. E. Schlichting & E. D. Young (2022) note the need to include estimates of the properties of H- and O-rich Fe-bearing metals at the extreme pressures present in the mantles and cores of sub-Neptunes. High-pressure behavior of the material that comprises planetary interiors remains poorly understood (e.g., B. Journaux et al. 2020). Furthermore, it is possible that core–mantle boundary temperatures may exceed the upper limit of 4000 K explored in this work (E. D. Young et al. 2024). However, we are unable to produce models at higher temperatures due to a complete lack of relevant laboratory data. We stress the need for further experiments to refine our knowledge of the fundamental quantities underpinning planetary interior and atmospheric models.

Alongside limitations to the magma–atmosphere interaction model, there are also caveats which apply to the upper atmospheric components of our modeling framework. `HELIOS` does not yet include the effect of H_2O–H_2O CIA (L. O. Anisman et al. 2022), which may be relevant due to the high H_2O abundances found by our models. Our modeling framework could also be improved by coupling the radiative transfer and photochemistry in a fully self-consistent manner; however this is not expected to alter major chemical trends (S. Mukherjee et al. 2025). As noted above, coupling to atmospheric escape models (e.g., C. Cherubim et al. 2025) will also be an important step toward predicting upper atmospheric composition, particularly at lower atmospheric pressures, which may be probed in high-resolution transmission spectroscopy. Additionally, although our framework iterates between a radiative–convective model and an equilibrium chemistry model with rainout condensation, allowing for feedback between the change in chemistry due to condensation and the temperature profile, it does not account for latent heat released by condensation, which can alter the temperature profile (R. T. Pierrehumbert 2010).

In addition to H_2O, CH_4, and CO_2, B. Benneke et al. (2024) find some evidence for the presence of CS_2 in the atmosphere of TOI-270 d, albeit with a low detection significance of 2.55σ. L. Felix et al. (2025) also found indications of sulfur-bearing species in this planet's atmosphere. We are unable to assess the likelihood of this species being present as a result of magma–atmosphere interactions, since sulfur-bearing species are not included in the chemical network of the H. E. Schlichting & E. D. Young (2022) model. Future expansion of the chemical network to include these species, along with nitrogen-bearing species as discussed previously, would enable a more complete picture of the atmospheric composition of atmospheres resulting from magma–atmosphere interactions.

At present, our model does not account for possible de-mixing between water and hydrogen in the deep atmosphere as proposed by, e.g., E. Bailey & D. J. Stevenson (2021) and A. Gupta et al. (2025). However, A. Gupta et al. (2025) suggest that de-mixing is unlikely to occur for TOI-270 d, meaning that this limitation should not impact our conclusions regarding this planet.

4.5. Conclusions

Interactions between sub-Neptune atmospheres and underlying magma oceans are expected to significantly impact atmospheric composition. We have developed a modeling framework to connect the magma–atmosphere interaction model constructed by H. E. Schlichting & E. D. Young (2022) to the upper, observable atmosphere. Using this framework, we generated models of the sub-Neptune TOI-270 d in which an initially solar-composition atmosphere is allowed to react with the mantle and core. We compared our results to JWST observations of the planet from B. Benneke et al. (2024), finding that it is possible to match its measured atmospheric composition, including the abundances of H_2O, CH_4, and CO_2. The model parameters leading to a best-fit solution are $T_{\mathrm{m-a}} = 3000$ K, $T_{\mathrm{c-m}} = 4000$ K, $x_{\mathrm{Fe}} = 33\%$, and $K_{zz} = 10^7$ cm^2 s^{-1}. We note that $x_{\mathrm{Fe}} = 33\%$ does not deviate from an Earth-like value, and that many other parameter combinations also provide a reasonable explanation for the planet's measured atmospheric composition. In general, magma–atmosphere interactions appear to enhance atmospheric metallicity while reducing C/O relative to solar values. This indicates that sub-Neptunes with metal-rich atmospheres do not necessarily form by accreting substantial amounts of icy material, and could instead be explained by the accretion of hydrogen-dominated nebular gas onto a molten rocky body.

This work represents an early step toward understanding just one process controlling how sub-Neptunes formed and evolved to their present-day states. Substantial further work is required to understand the relative contributions affecting sub-Neptune atmospheric composition and evolution. However, with a combination of new modeling efforts and high-quality spectra

now available from JWST, the promise of uncovering the nature of these mysterious worlds has never been greater.

Acknowledgments

The authors thank the anonymous referee for their careful review of this manuscript. This research was supported by the AEThER program, funded in part by the Alfred P. Sloan Foundation under grant #G202114194, as well as by NASA ADAP 80NSSC19K1014. The authors thank Anat Shahar, the Principal Investigator of the AEThER collaboration, as well as other collaboration members for fruitful discussion that helped to shape many of the ideas behind this work. M.N. thanks the Heising–Simons Foundation for their funding through the 51 Pegasi b Postdoctoral Fellowship. This research has made use of the NASA Astrophysics Data System and the NASA Exoplanet Archive. Thermodynamic data required for the magma–atmosphere interaction model were provided in part by the National Institute of Standards and Technology Standard Reference Data Program.

Software: NUMPY (C. R. Harris et al. 2020), SCIPY (P. Virtanen et al. 2020), MATPLOTLIB (J. D. Hunter 2007).

ORCID iDs

Matthew C. Nixon https://orcid.org/0000-0001-8236-5553
R. Sander Somers https://orcid.org/0009-0008-1115-8774
Arjun B. Savel https://orcid.org/0000-0002-2454-768X
Jegug Ih https://orcid.org/0000-0003-2775-653X
Eliza M.-R. Kempton https://orcid.org/0000-0002-1337-9051
Edward D. Young https://orcid.org/0000-0002-1299-0801
Hilke E. Schlichting https://orcid.org/0000-0002-0298-8089
Tim Lichtenberg https://orcid.org/0000-0002-3286-7683
Luis Welbanks https://orcid.org/0000-0003-0156-4564
William Misener https://orcid.org/0000-0001-6315-7118
Anjali A. A. Piette https://orcid.org/0000-0002-4487-5533
Nicholas F. Wogan https://orcid.org/0000-0002-0413-3308

References

Amundsen, D. S., Tremblin, P., Manners, J., Baraffe, I., & Mayne, N. J. 2017, A&A, 598, A97
Andrae, R., Schulze-Hartung, T., & Melchior, P. 2010, arXiv:1012.3754
Anisman, L. O., Chubb, K. L., Changeat, Q., et al. 2022, JQSRT, 283, 108146
Asplund, M., Grevesse, N., Sauval, A. J., & Scott, P. 2009, ARA&A, 47, 481
Azzam, A. A. A., Tennyson, J., Yurchenko, S. N., & Naumenko, O. V. 2016, MNRAS, 460, 4063
Badro, J., Brodholt, J. P., Piet, H., Siebert, J., & Ryerson, F. J. 2015, PNAS, 112, 12310
Bailey, E., & Stevenson, D. J. 2021, PSJ, 2, 64
Barber, R. J., Strange, J. K., Hill, C., et al. 2014, MNRAS, 437, 1828
Barin, I. 1995, Thermochemical Data of Pure Substances (Weinheim: VCH Verlagsgesellschaft mbH)
Barton, E. J., Yurchenko, S. N., & Tennyson, J. 2013, MNRAS, 434, 1469
Beatty, T. G., Welbanks, L., Schlawin, E., et al. 2024, ApJL, 970, L10
Benneke, B., Roy, P.-A., Coulombe, L.-P., et al. 2024, arXiv:2403.03325
Breza, B., Nixon, M. C., Kempton, E. M. R., et al. 2025, ApJL, 993, L46
Burrows, A., & Sharp, C. M. 1999, ApJ, 512, 843
Chase, M. 1998, NIST-JANAF Thermochemical Tables, Vol. 1 (4th ed.; Meliville, NY: AIP)
Chen, H., & Rogers, L. A. 2016, ApJ, 831, 180
Cherubim, C., Wordsworth, R., Bower, D. J., et al. 2025, ApJ, 983, 97
Chubb, K. L., Naumenko, O., Keely, S., et al. 2018, JQSRT, 218, 178
Chubb, K. L., Tennyson, J., & Yurchenko, S. N. 2020, MNRAS, 493, 1531
Coles, P. A., Yurchenko, S. N., & Tennyson, J. 2019, MNRAS, 490, 4638
Davenport, B., Kempton, E. M. R., Nixon, M. C., et al. 2025, ApJL, 984, L44
Dykyj, J., Svoboda, J., Wilhoit, R. C., & Hall, K. R. 2001, Landolt-Börnstein —Group IV Physical Chemistry, Vol. 20C, Vapor Pressure and Antoine Constants for Nitrogen Containing Organic Compounds (Cham: Springer)
Fegley, B., & Cameron, A. G. W. 1987, E&PSL, 82, 207
Felix, L., Kitzmann, D., Demory, B.-O., & Mordasini, C. 2025, A&A, 701, A296
France, K., Loyd, R. O. P., Youngblood, A., et al. 2016, ApJ, 820, 89
Fulton, B. J., Petigura, E. A., Howard, A. W., et al. 2017, AJ, 154, 109
Gail, H. P., Wetzel, S., Pucci, A., & Tamanai, A. 2013, A&A, 555, A119
Gaillard, F., Bernadou, F., Roskosz, M., et al. 2022, E&PSL, 577, 117255
Gao, P., Piette, A. A. A., Steinrueck, M. E., et al. 2023, ApJ, 951, 96
Ginzburg, S., Schlichting, H. E., & Sari, R. 2016, ApJ, 825, 29
Glein, C. R., Yu, X., & Luu, C. N. 2025, ApJ, 985, 187
Goodwin, R. D. 1985, JPCRD, 14, 849
Gordon, I. E., Rothman, L. S., Hargreaves, R. J., et al. 2022, JQSRT, 277, 107949
Grimm, S. L., Malik, M., Kitzmann, D., et al. 2021, ApJS, 253, 30
Günther, M. N., Pozuelos, F. J., Dittmann, J. A., et al. 2019, NatAs, 3, 1099
Gupta, A., & Schlichting, H. E. 2019, MNRAS, 487, 24
Gupta, A., Stixrude, L., & Schlichting, H. E. 2025, ApJL, 982, L35
Haar, L., & Gallagher, J. S. 1978, JPCRD, 7, 635
Hansen, B. M. S. 2008, ApJS, 179, 484
Hargreaves, R. J., Gordon, I. E., Rey, M., et al. 2020, ApJS, 247, 55
Harris, C. R., Millman, K. J., van der Walt, S. J., et al. 2020, Natur, 585, 357
Heng, K., Owen, J. E., & Tian, M. 2025, ApJ, 994, 28
Hirschmann, M. M. 2016, AmMin, 101, 540
Hirschmann, M. M., Withers, A. C., Ardia, P., & Foley, N. T. 2012, E&PSL, 345, 38
Holmberg, M., & Madhusudhan, N. 2024, A&A, 683, L2
Hu, R., Damiano, M., Scheucher, M., et al. 2021, ApJL, 921, L8
Hunter, J. D. 2007, CSE, 9, 90
Husser, T. O., Wende-von Berg, S., Dreizler, S., et al. 2013, A&A, 553, A6
Journaux, B., Kalousová, K., Sotin, C., et al. 2020, SSRv, 216, 7
Kempton, E. M. R., Lessard, M., Malik, M., et al. 2023a, ApJ, 953, 57
Kempton, E. M. R., Zhang, M., Bean, J. L., et al. 2023b, Natur, 620, 67
Kite, E. S., Fegley, B., Jr., Schaefer, L., & Ford, E. B. 2019, ApJL, 887, L33
Kite, E. S., Fegley, B., Jr., Schaefer, L., & Ford, E. B. 2020, ApJ, 891, 111
Kitzmann, D., Stock, J. W., & Patzer, A. B. C. 2024, MNRAS, 527, 7263
Kurucz, R. L., & Bell, B. 1995, Kurucz CD-ROM, Atomic Line List (Cambridge, MA: Smithsonian Astrophysical Observatory)
Lichtenberg, T. 2021, ApJL, 914, L4
Lichtenberg, T., & Clement, M. S. 2022, ApJL, 938, L3
Lichtenberg, T., & Miguel, Y. 2025, TrGeo, 7, 51
Lide, D. 2009, CRC Handbook of Chemistry and Physics (90th ed.; Boca Raton, FL: CRC Press)
Loyd, R. O. P., France, K., Youngblood, A., et al. 2016, ApJ, 824, 102
Luque, R., & Pallé, E. 2022, Sci, 377, 1211
Madhusudhan, N., Nixon, M. C., Welbanks, L., Piette, A. A. A., & Booth, R. A. 2020, ApJL, 891, L7
Madhusudhan, N., Sarkar, S., Constantinou, S., et al. 2023, ApJL, 956, L13
Malik, M., Grosheintz, L., Mendonça, J. M., et al. 2017, AJ, 153, 56
Malik, M., Kempton, E. M. R., Koll, D. D. B., et al. 2019a, ApJ, 886, 142
Malik, M., Kitzmann, D., Mendonça, J. M., et al. 2019b, AJ, 157, 170
Mikal-Evans, T., Madhusudhan, N., Dittmann, J., et al. 2023, AJ, 165, 84
Misener, W., Schlichting, H. E., & Young, E. D. 2023, MNRAS, 524, 981
Moore, G., Vennemann, T., & Carmichael, I. S. E. 1998, AmMin, 83, 36
Mordasini, C., Alibert, Y., & Benz, W. 2009, A&A, 501, 1139
Moses, J. I., Allen, M., & Yung, Y. L. 1992, Icar, 99, 318
Moses, J. I., Fouchet, T., Bézard, B., et al. 2005, JGRE, 110, E08001
Moses, J. I., Line, M. R., Visscher, C., et al. 2013, ApJ, 777, 34
Mukherjee, S., Fortney, J. J., Wogan, N. F., Sing, D. K., & Ohno, K. 2025, ApJ, 985, 209
Murphy, D. M., & Koop, T. 2005, QJRMS, 131, 1539
Nicholls, H., Lichtenberg, T., Bower, D. J., & Pierrehumbert, R. 2024, JGRE, 129, 2024JE008576
Nicholls, H., Pierrehumbert, R. T., Lichtenberg, T., Soucasse, L., & Smeets, S. 2025, MNRAS, 536, 2957
Nixon, M. C., & Madhusudhan, N. 2020, MNRAS, 496, 269
Nixon, M. C., & Madhusudhan, N. 2021, MNRAS, 505, 3414
Nixon, M. C., & Madhusudhan, N. 2022, ApJ, 935, 73
Nixon, M. C., Welbanks, L., McGill, P., & Kempton, E. M. R. 2024a, ApJ, 966, 156
Nixon, M. C., Piette, A. A. A., Kempton, E. M. R., et al. 2024b, ApJL, 970, L28
Okuchi, T. 1997, Sci, 278, 1781
Owen, J. E., & Wu, Y. 2017, ApJ, 847, 29
Owens, A., Yachmenev, A., Thiel, W., Tennyson, J., & Yurchenko, S. N. 2017, MNRAS, 471, 5025
Pan, V., Holloway, J. R., & Hervig, R. L. 1991, GeCoA, 55, 1587
Piaulet-Ghorayeb, C., Benneke, B., Radica, M., et al. 2024, ApJL, 974, L10

Pierrehumbert, R. T. 2010, Principles of Planetary Climate (Cambridge: Cambridge Univ. Press)
Pineda, J. S., Youngblood, A., & France, K. 2021, ApJ, 918, 40
Pinhas, A., Rackham, B. V., Madhusudhan, N., & Apai, D. 2018, MNRAS, 480, 5314
Polyansky, O. L., Kyuberis, A. A., Zobov, N. F., et al. 2018, MNRAS, 480, 2597
Prydz, R., & Goodwin, R. D. 1972, JChTh, 4, 127
Richard, C., Gordon, I., Rothman, L., et al. 2012, JQSRT, 113, 1276
Rigby, F. E., Pica-Ciamarra, L., Holmberg, M., et al. 2024, ApJ, 975, 101
Rogers, J. G., Schlichting, H. E., & Owen, J. E. 2023, ApJL, 947, L19
Rogers, L. A. 2015, ApJ, 801, 41
Rothman, L. S., Gordon, I. E., Barber, R. J., et al. 2010, JQSRT, 111, 2139
Schaefer, L., Wordsworth, R. D., Berta-Thompson, Z., & Sasselov, D. 2016, ApJ, 829, 63
Schlawin, E., Ohno, K., Bell, T. J., et al. 2024, ApJL, 974, L33
Schlichting, H. E., & Young, E. D. 2022, PSJ, 3, 127
Schulik, M., & Booth, R. A. 2023, MNRAS, 523, 286
Seo, C., Ito, Y., & Fujii, Y. 2024, ApJ, 975, 14
Sharp, C. M., & Huebner, W. F. 1990, ApJS, 72, 417
Shorttle, O., Jordan, S., Nicholls, H., Lichtenberg, T., & Bower, D. J. 2024, ApJL, 962, L8
Sousa-Silva, C., Al-Refaie, A. F., Tennyson, J., & Yurchenko, S. N. 2015, MNRAS, 446, 2337
Stock, J. W., Kitzmann, D., Patzer, A. B. C., & Sedlmayr, E. 2018, MNRAS, 479, 865
Stock, J. W., Kitzmann, D., & Patzer, A. B. C. 2022, MNRAS, 517, 4070
Tang, Y., Fortney, J. J., Nimmo, F., et al. 2025, ApJ, 989, 28
Tsai, S.-M., Innes, H., Lichtenberg, T., et al. 2021, ApJL, 922, L27
Van Eylen, V., Astudillo-Defru, N., Bonfils, X., et al. 2021, MNRAS, 507, 2154
Virtanen, P., Gommers, R., Oliphant, T. E., et al. 2020, NatMe, 17, 261
Wagner, W., & Kretzschmar, H.-J. 2008, International Steam Tables: Properties of Water and Steam Based on the Industrial Formulation IAPWS-IF97 (Berlin: Springer)
Welbanks, L., & Madhusudhan, N. 2021, ApJ, 913, 114
Welbanks, L., Bell, T. J., Beatty, T. G., et al. 2024, Natur, 630, 836
Werlen, A., Dorn, C., Schlichting, H. E., Grimm, S. L., & Young, E. D. 2025, ApJL, 988, L55
Wogan, N. 2024, Nicholaswogan/photochem: photochem, v0.6.2, Zenodo, doi: 10.5281/zenodo.14032108
Wogan, N. F., Catling, D. C., Zahnle, K. J., & Lupu, R. 2023, PSJ, 4, 169
Wogan, N. F., Batalha, N. E., Zahnle, K. J., et al. 2024, ApJL, 963, L7
Wogan, N. F., Batalha, N. E., Zahnle, K., et al. 2025, PSJ, 6, 256
Yaws, C. L. 1999, Chemical Properties Handbook: Physical, Thermodynamic, Environmental, Transport, Safety and Health Related Properties for Organic and Inorganic Chemicals (New York: McGraw-Hill)
Young, E. D., Stixrude, L., Rogers, J. G., Schlichting, H. E., & Marcum, S. P. 2024, PSJ, 5, 268
Youngblood, A., France, K., Loyd, R. O. P., et al. 2016, ApJ, 824, 101
Yu, X., Moses, J. I., Fortney, J. J., & Zhang, X. 2021, ApJ, 914, 38
Zahnle, K., Marley, M. S., Morley, C. V., & Moses, J. I. 2016, ApJ, 824, 137